Chapter 11

Determination of Stress from Faults

Structural geologists observe deformations of rocks. However, they infer or constrain (paleo)stresses from faults. It is important to know not only the deformation but also the state of stress when the deformation occurs for the understanding of the mechanics of tectonics. In this chapter we study the methods for (paleo)stress analysis. The methods are useful to understand the present state of stress when they are applied to seismological data. In addition, the (paleo)stress field is important to understand the migration of fluids, including hydrocarbons and thermal water. Theories based on the Wallace-Bott hypothesis are introduced in the first half of this chapter. The sections after Section 11.6 introduce other theories on the relationship between faulting, stress, and deformation.

11.1 Mesoscale faults

We observe fault on various scales at outcrops. Mesoscale faults are minor faults with displacements that can be grasped at one outcrop (Fig. 11.1), i.e., their displacements range from a few millimeters to several meters. The slip orientation of a fault is recognized by the scratches or grooves produced by fault movement on a fault surface. They are called *fault striations* or simply *striae* (Fig. 11.2). Offset of pre-faulting features such as strata tells the sense of shear (Fig. 11.1). Mesoscale faults can be reactivated. Those faults have two or a few sets of striae with different orientations. For the overlapping striae, the sense of shear can be identified for each set by asymmetrical minor structures along the striae [181]. It is possible to determine the relative chronology of the sets by their overlapping relationship. Consequently, one can recognize not only the orientation of a fault surface but the sense of shear and slip direction for each mesoscale fault. These are referred to as *fault-slip data*.

For the following reasons, those faults are more often used than large-scale faults to investigate the stresses responsible for the movement of the faults. Firstly, the much greater number density of those faults than that of large-scale faults allows us to infer a stress field with a higher spatial resolution. Secondly, most large faults have a complicated history as they are sometimes reactivated and a large amount of work is needed to understand that history. Minor faults can be reactivated, but their history is believed to be simple. Repeated reactivation of a fault increases its total displacement,

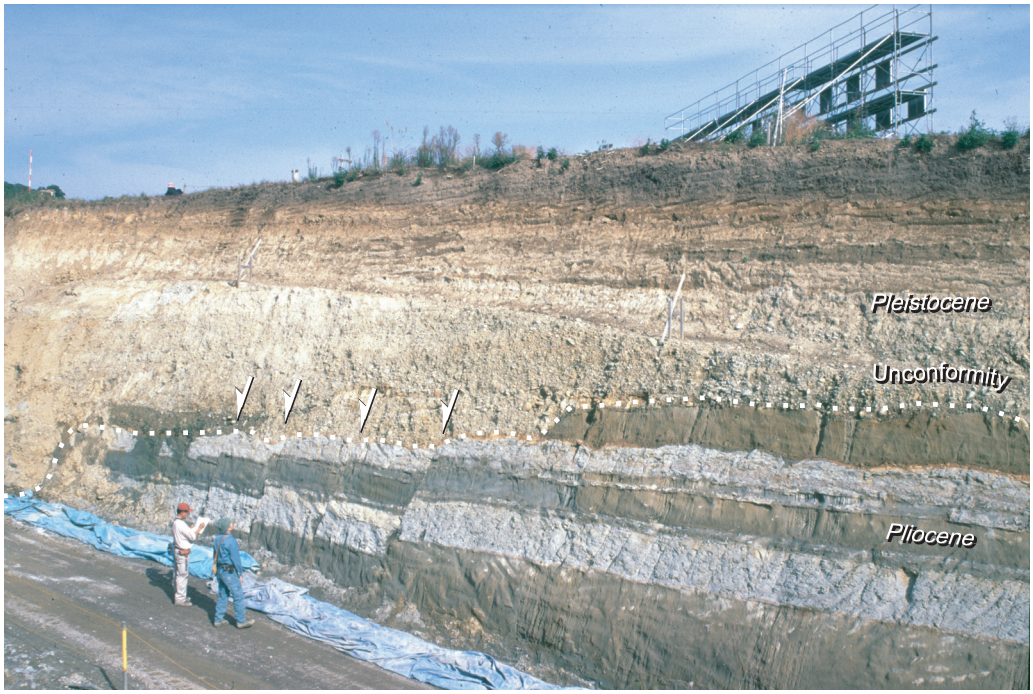

Figure 11.1: Mesoscale faults (arrows) in Pliocene forearc sediments, the Miyazaki Group, northern Ryukyu arc, Japan [266]. The sediments and the faults are truncated by the angular unconformity (dotted line) on which Quaternary gravel layers lie, indicating that the faulting is older than the formation of the unconformity.

but mesoscale faults have small displacements. Thirdly, the deformation of a rock mass caused by a mesoscale fault within the mass can be treated as an infinitesimal deformation if the rock mass is very large (§2.7).

The techniques introduced in this chapter utilize fault-slip data obtained from outcrops and oriented borehole cores to constrain (paleo)stresses. If those faults were generated by the present stress field, the stress that they indicate is the present stress. The same techniques can be applied to seismological data to infer the present stress.

Several methods have been proposed to estimate the state of stress from faults. Among them, the most popular one is Anderson's theory of faulting [4]. The theory is still used, as it is very simple. However, one can trace modern methods back to the papers of the 1950s by Wallace and Bott [20, 252]. Bott [20] explained the abundance of oblique slip faults, which were incompatible with Anderson's theory (§6.3). McKenzie utilized Bott's principle to infer the state of stress at an earthquake source [137]. The principle was used to formulate a mathematical inverse method by Carey and Brunier [35] and by Angelier [6] in the 1970s to infer paleostresses from geological

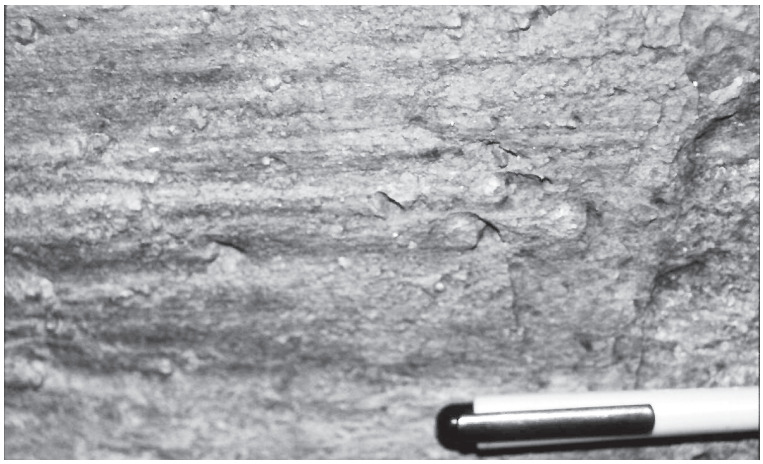

Figure 11.2: Fault striations on a fault surface in Early Miocene strata, the Atsumi Formation, Northeast Japan. There are comet-like structures heading right. They were produced by the drag of hard particles between fault surfaces. These asymmetric structures indicate that this fault is dextral in sense, i.e., the block on this side of the fault moved left.

faults. The inverse method was applied to many areas in the world. Since the mid 1990s, theoretical investigations have been carried out on the numerical techniques to separate stresses from fault data that record plural stresses [60, 161, 209, 264].

11.2 Wallace-Bott hypothesis

11.2.1 Basic equations

Modern methods for determining (paleo)stresses are based on the Wallace-Bott hypothesis [20, 252], stating that the shear traction applied on a given fault plane causes a slip in the direction and orientation of that shear traction, irrespective of the faults created in an intact rock or along a pre-existing fracture.

The traction vector at the fault plane whose unit normal is $\boldsymbol{n}$ is given by the equation

$$\boldsymbol{t}(\boldsymbol{n}) = \boldsymbol{\sigma} \cdot \boldsymbol{n}. \tag{11.1}$$

From Eqs. (3.16) and (3.17), the normal and tangential components of this vector are the normal and shear traction vectors

$$\boldsymbol{\sigma}_{\mathrm{N}} = \mathbf{N} \cdot \boldsymbol{\sigma} \cdot \boldsymbol{n} = \boldsymbol{n}\big[\boldsymbol{n} \cdot (\boldsymbol{\sigma} \cdot \boldsymbol{n})\big] \tag{11.2}$$

$$\boldsymbol{\sigma}_{\mathrm{S}} = (\mathbf{I} - \mathbf{N}) \cdot \boldsymbol{\sigma} \cdot \boldsymbol{n} = \boldsymbol{\sigma} \cdot \boldsymbol{n} - \boldsymbol{n}\big[\boldsymbol{n} \cdot (\boldsymbol{\sigma} \cdot \boldsymbol{n})\big]. \tag{11.3}$$

Faulting occurs to release the shear stress so the slip direction is indicated by the unit vector $-\boldsymbol{\sigma}_S/|\boldsymbol{\sigma}_S|$ instead of $\boldsymbol{\sigma}_S$.

The slip direction of a given fault has a linear relationship with the stress tensor $\boldsymbol{\sigma}$. To see this, let us rewrite Eq. (11.3) as $\boldsymbol{\sigma}_S = f(\boldsymbol{\sigma}, \boldsymbol{n})$. Then the linearity is represented by the equation $f(a_1\boldsymbol{\sigma}^{(1)} + a_2\boldsymbol{\sigma}^{(2)}, \boldsymbol{n}) = a_1 f(\boldsymbol{\sigma}^{(1)}, \boldsymbol{n}) + a_2 f(\boldsymbol{\sigma}^{(2)}, \boldsymbol{n})$, where $\boldsymbol{\sigma}_S^{(1)}$ and $\boldsymbol{\sigma}_S^{(2)}$ are stress tensors and a_1 and a_2 are arbitrary scalar variables. Equation (11.3) is rewritten for these tensors as

$$\begin{aligned}\boldsymbol{\sigma}_S^{(1)} &= (\boldsymbol{I} - \boldsymbol{N}) \cdot \boldsymbol{\sigma}^{(1)} \cdot \boldsymbol{n},\\ \boldsymbol{\sigma}_S^{(2)} &= (\boldsymbol{I} - \boldsymbol{N}) \cdot \boldsymbol{\sigma}^{(2)} \cdot \boldsymbol{n},\end{aligned}$$

so that we have

$$\begin{aligned}a_1\boldsymbol{\sigma}_S^{(1)} + a_2\boldsymbol{\sigma}_S^{(2)} &= a_1(\boldsymbol{I} - \boldsymbol{N}) \cdot \boldsymbol{\sigma}^{(1)} \cdot \boldsymbol{n} + a_2(\boldsymbol{I} - \boldsymbol{N}) \cdot \boldsymbol{\sigma}^{(2)} \cdot \boldsymbol{n}\\ &= \boldsymbol{\sigma}_S = (\boldsymbol{I} - \boldsymbol{N}) \cdot \left[a_1\boldsymbol{\sigma}^{(1)} + a_2\boldsymbol{\sigma}^{(2)}\right] \cdot \boldsymbol{n}.\end{aligned}$$

Consequently, the slip direction predicted by the Wallace-Bott hypothesis has a linear relationship with stress tensors.

11.2.2 Graphical expressions of slip directions

The slip direction predicted by the Wallace-Bott hypothesis for a given fault and a stress is shown by Means' graphical method[1] [142]. A tangent-lineation diagram is a graphical expression of fault-slip data and is convenient for theoretical considerations.

Means' graphical method Suppose that a state of stress and a fault orientation are given, and that the vector $\boldsymbol{s}$ points to the slip direction on the fault by the stress. The vector is obtained through the following steps. Firstly, the stress axes are plotted on a stereonet whose center indicates the pole to the fault (Fig. 11.3). The point P on the stereonet denotes the pole. Secondly, let δ_1 be the angular distance between the σ_1-axis and the pole, and δ_3 be that between the σ_3-axis and the pole. We calculate the parameters

$$a^{(1)} = \frac{1}{2}(\sigma_1 - \sigma_2)\sin 2\delta_1, \tag{11.4}$$

$$a^{(3)} = \frac{1}{2}(\sigma_2 - \sigma_3)\sin 2\delta_3. \tag{11.5}$$

Thirdly, the arrows for the unit vectors $\boldsymbol{u}^{(1)}$ and $\boldsymbol{u}^{(2)}$ are drawn from the point P. The former is directed on the opposite side of the σ_1-orientation on the stereonet. The latter is directed from the point P to the σ_3-orientation. Using the parameters defined by Eqs. (11.4) and (11.5), we produce the vectors $\boldsymbol{s}^{(1)} = a^{(1)}\boldsymbol{u}^{(1)}$ and $\boldsymbol{s}^{(3)} = a^{(3)}\boldsymbol{u}^{(3)}$ and draw them on the stereonet (Fig. 11.3). Finally, the point S is plotted on the base circle of the stereonet, where the ray PS is parallel to the vector $\boldsymbol{s} = \boldsymbol{s}^{(1)} + \boldsymbol{s}^{(3)}$. The point S indicates the slip direction on the fault plane by the given stress.

[1] An exercise at the end of this chapter takes up the theoretical basis for this method.

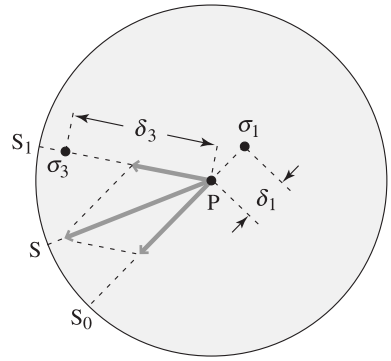

Figure 11.3: Graphical method to determine the slip direction of a fault whose pole is plotted at the center of a stereonet.

Equations (11.4) and (11.5) demonstrate that the slip direction depends not only on the orientation of stress axes but also on the ratio

$$R = \frac{\sigma_1 - \sigma_2}{\sigma_2 - \sigma_3}. \tag{11.6}$$

This is related to the stress ratio as $R = \Phi/(1-\Phi)$, i.e., the slip direction depends on Φ. If the ratio is zero, the ray PS_0 indicates the slip direction. The ray PS_1 indicates the slip direction for the case of $\Phi = 1$. It should be stressed that Φ influences the slip direction as much as the principal stress orientations do.

The graphical method demonstrates that slip directions are directed away from the σ_1-axis and toward the σ_3-axis. If the fault in Fig. 11.3 is nearly perpendicular to the σ_2-axis, the angles δ_1 and δ_3 are approximately equal to 90°. Therefore, $a^{(1)} \approx a^{(3)} \approx 0$, though their signs depend on the tiny difference of the angles from 90°. This further indicates that the slip direction, $\boldsymbol{s}$, is swerved around the σ_2-axis.

Tangent-lineation diagram A tangent-lineation diagram is a convenient graphical method to illustrate the slip directions.

The plane containing the slip vector and the pole to the fault plane is called the *M-plane* of the fault. The plane perpendicular to the M- and fault planes is know as an *auxiliary plane* (Fig. 11.4(a)). A fault-slip datum is expressed in the diagram by an arrow plotted on a lower-hemisphere stereonet (Fig. 11.4(b)). The position of the arrow in the stereonet indicates the pole to the fault plane. The arrow is drawn parallel to the M-plane, and is pointing at the slip direction of the footwall.

Figure 11.5 shows tangent-lineation diagrams for five different stress ratios but with common principal stress axes. The pattern made up of arrows on a diagram shows a source and sink at the σ_1- and σ_3-axes, respectively[2]. As the cases $\Phi = 0$ and 1 indicate axial stresses, the pattern for those

[2]The source and sink are called *fabric attractors* in metamorphic geology [175].

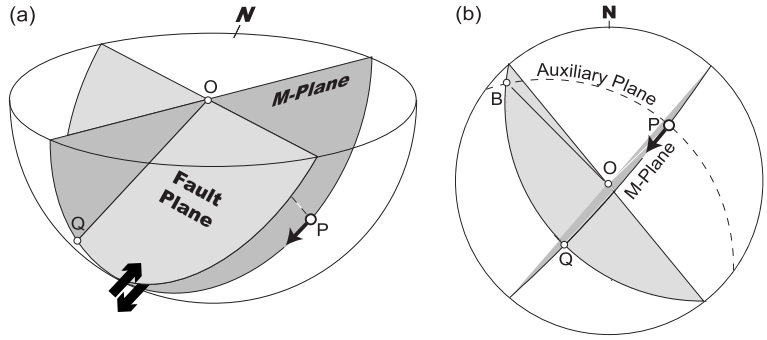

Figure 11.4: (a) Schematic picture showing the orientation of a reverse fault plane and the direction of fault movement (bold arrows). The line OQ indicates the orientation of striae, and the point P is the pole to the fault plane. The arrow attached to the point P indicates the slip direction of the footwall block. The plane containing the triangle OPQ is called the M-plane for the fault. The plane perpendicular to the fault plane and M-plane is called the auxiliary plane. (b) Lower-hemisphere stereonet showing the three planes and the slip direction of the footwall that is depicted by the arrow attached to the point P. The line OB is the intersection of the fault and auxiliary plane.

cases shows axial symmetry about the σ_1- and σ_3-axis, respectively. The pattern exhibits orthorhombic symmetry for triaxial stresses, and a saddle point appears at the σ_2-orientation. Tangent-lineation diagram for a set of natural fault-slip data is shown in Fig. 11.6.

11.2.3 Indeterminacy of stress from faults

Fault-slip data constrain the state of stress that was responsible for the faults. However, not all the stress components are determined. The Wallace-Bott hypothesis indicates that slip directions are not affected by pore fluid pressure, although it controls the strength of faults. The effective stress is given by the equation $\boldsymbol{\sigma}' = \boldsymbol{\sigma} - p\boldsymbol{I}$. Thanks to the linearity, the slip direction due to $\boldsymbol{\sigma}'$ is the linear combination of those by $\boldsymbol{\sigma}$ and $-p\boldsymbol{I}$. However, the latter is an isotropic stress and causes no shear traction. Therefore, the pore fluid pressure does not affect the slip direction of a fault. This is convenient for paleostress analysis, because it is difficult to know the pore fluid pressure on a fault surface when the fault moved.

It is also difficult to estimate the depth of burial of a fault when it was activated. However, the depth has little affect on the slip direction. Crustal stress is limited by the brittle strength (§6.7), and faulting occurs when stress is brought to the limit. Equation (6.21) indicates that the limiting stress is proportional to the depth z. Let $\boldsymbol{\sigma}_0$ be an arbitrary stress tensor. Since the slip directions due to stresses $\boldsymbol{\sigma}_0$ and $\boldsymbol{\sigma} = q\boldsymbol{\sigma}_0$ are the same, the slip directions are independent from the depth of burial. However, this is valid only as an approximation, because stress states inferred by in-situ measurements more or less deviate from the proportionality.

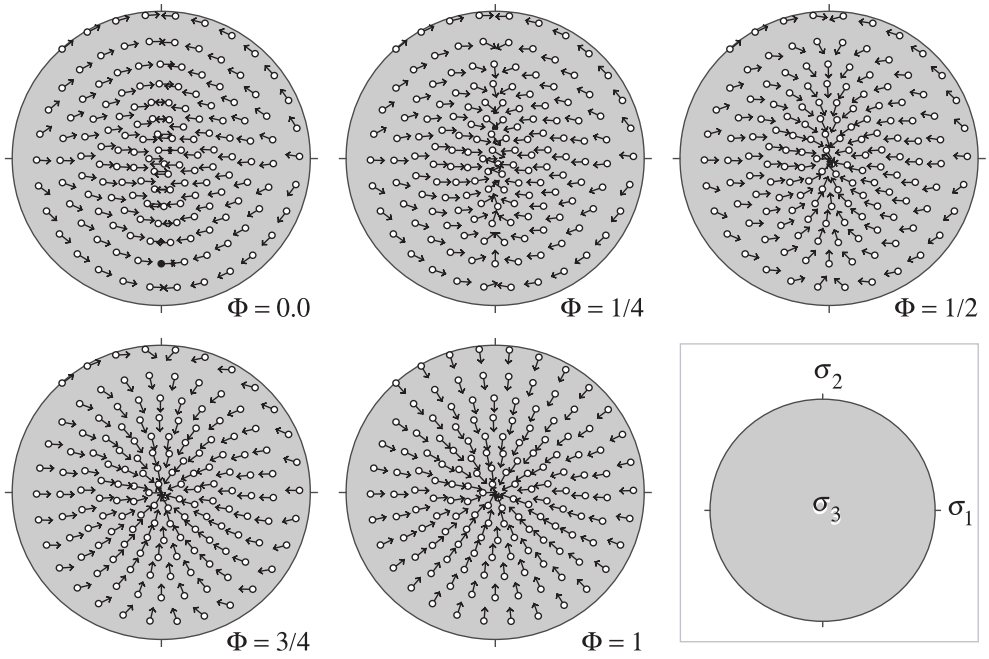

Figure 11.5: Tangent-lineation diagrams showing the slip directions of faults by stresses with the same principal orientations but different stress ratios. The principal orientations are shown in the lower right box. Open circles in the stereonets indicate the poles to the fault plane.

The slip directions predicted by the Wallace-Bott hypothesis for the stresses $\boldsymbol{\sigma}$ and

$$\boldsymbol{\sigma} = q\boldsymbol{\sigma}_0 - p\boldsymbol{I} \tag{11.7}$$

are the same for a given fault, whether or not p and q are interpreted as pore pressure and depth. When the state of stress is illustrated by Mohr circles, p and q indicate the position of the circles on the abscissa and the size of the circles, respectively. The stresses that have common principal orientations and similar stress ellipsoids have similar Mohr circles, and result in identical slip directions. The tensor that represents those stresses is termed *reduced stress tensor*.

Due to the insensibility of the slip direction to these parameters, fault-slip it is not enough to constrain the mean and differential stresses. However, this is convenient for paleostress analysis, because we do not need to worry about the depth and pore fluid pressure when each fault was activated[3]. These quantities are difficult to estimate.

It is convenient to assume a special form for $\boldsymbol{\sigma}_0$ to consider slip directions. For example, we can

[3]Researchers have attempted to determine all the stress components from fault-slip data with assumption such as the brittle strength of rocks [8].

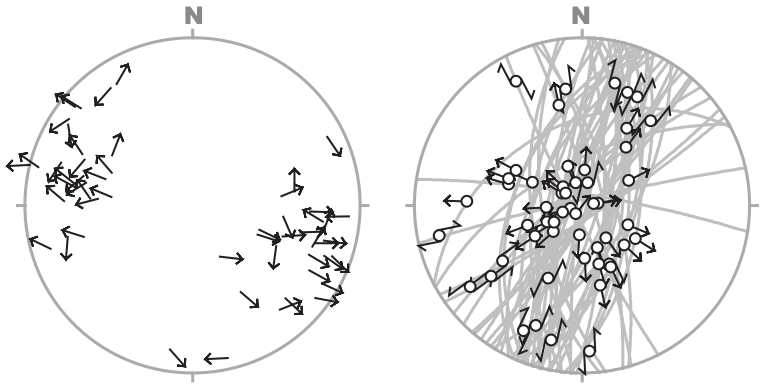

Figure 11.6: Natural fault-slip data obtained from the Otadai Formation, mid Quaternary forearc basin deposit in central Japan [151]. The left panel is the tangent-lineation diagram showing the data. The right panel is the lower-hemisphere stereonet in which the orientations of fault planes are indicated by great circles. Open circles on the great circles designate the orientation of fault striations, and arrows attached to the open circles show the sense of shear. If an arrow is attached, it indicates the slip direction of the hanging wall. If two arrows are attached to an open circle, the arrows depict the sinistral or dextral sense of shear.

express any stress tensor by combining Eq. (11.7) and

$$\boldsymbol{\sigma}_0 = \boldsymbol{R}^{\mathrm{T}} \cdot \begin{pmatrix} 1 & 0 & 0 \\ 0 & \Phi & 0 \\ 0 & 0 & 0 \end{pmatrix} \cdot \boldsymbol{R}, \tag{11.8}$$

where $\boldsymbol{R}$ indicates the principal stress orientations and $\Phi = (\sigma_2 - \sigma_3)/(\sigma_1 - \sigma_3)$ is the stress ratio. The tensor between $\boldsymbol{R}^{\mathrm{T}}$ and $\boldsymbol{R}$ in Eq. (11.8) is a reduced stress tensor, but the definition of a reduced stress tensor is not unique [7]. Different shapes of reduced tensor is introduced in Section 11.5 and in Appendix B.

The tensor $\boldsymbol{\sigma}_0$ in the shape of Eq. (11.8) is enough to calculate the slip directions of faults. The orthogonal tensor $\boldsymbol{R}$ has three degrees of freedom corresponding to the three Euler angles (Fig. C.5). The reduced stress tensor has one degree of freedom. Therefore, $\boldsymbol{\sigma}_0$ has four degrees of freedom. However, the stress tensor has six degrees of freedom. The difference corresponds to p and q in Eq. (11.7). The tensor $\boldsymbol{\sigma}_0$ represents the principal orientations and stress ratio. In this chapter, the term "a state of stress" is used to denote the stresses with a common $\boldsymbol{\sigma}_0$.

A fault-slip datum does not tightly constrain the principal stress orientations. It should be noted that different stresses can result in a fault-slip datum. The admissible orientations for the datum are illustrated in Fig. 11.7. The possible principal σ_1 orientation reduces by a decrease of stress ratio, which in turn expands the possible σ_3 orientation. It is known that both the σ_1- and σ_3-axes exist on one side of the plane AOC [122]. Namely, if the domain OBC in Fig. 11.7 has the σ_1-axis, then the

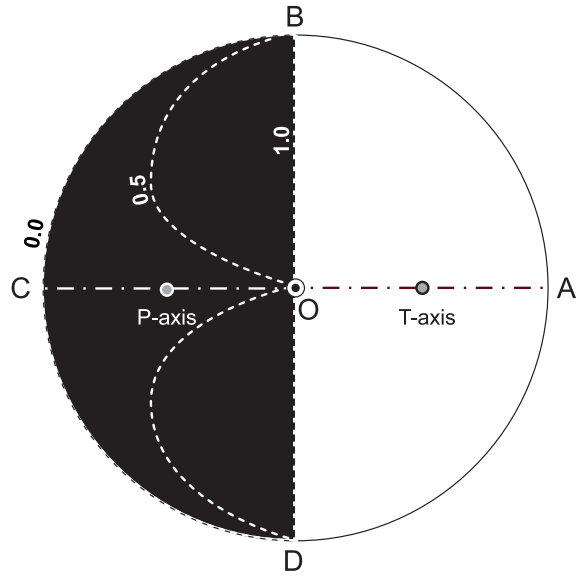

Figure 11.7: Stereogram (upper hemisphere) showing the principal stress orientations compatible with a fault-slip datum. The upper block is assumed to move rightwards on the plane ABCD. P- and T-axes are contained in the plane AOC and make angles of 45° with O. They approximate the σ_1- and σ_3-orientations if the Coulomb-Navier criterion holds for this fault. The Wallace-Bott hypothesis predicts the σ_1-axis in the region OBCD for this fault. The σ_3-axis is oriented in the region OBAD. The σ_1-orientation is constrained more tightly for a prescribed stress ratio. Dotted lines with decimal fractions show the rightward limit of the permissible region for the σ_1-axis, where the fractions indicate stress ratios. The lines are obtained from Eq. D.45.

σ_3-axis must exist in the domain OAB.

For example, if there are conjugated N–S trending normal faults formed by the E–W extensional stress with $\Phi = 0.5$ (Fig. 11.8(a)), the stress compatible with the fault-slip data is not unique. Stresses with a wide variation of principal orientations and stress ratios are compatible with the data. However, if there are varieties of fault attitudes and of slip directions, the admissible stresses are constrained as the overlapping region of the dotted and hatched regions in Fig. 11.8(a).

Figure 11.8(b) shows the case of two conjugated normal faults with different ages and different extensional orientations. If we do not know the difference and we regard them as the results of the same state of stress, the vertical axial compression is a possible stress compatible with the data, i.e., it is not possible to distinguish from the data which scenario is correct, the two-phase or the single-phase stress history. The set of stress states compatible with given data set are said to be associated stresses [264]. Other lines of evidence are needed to determine the correct stresses.

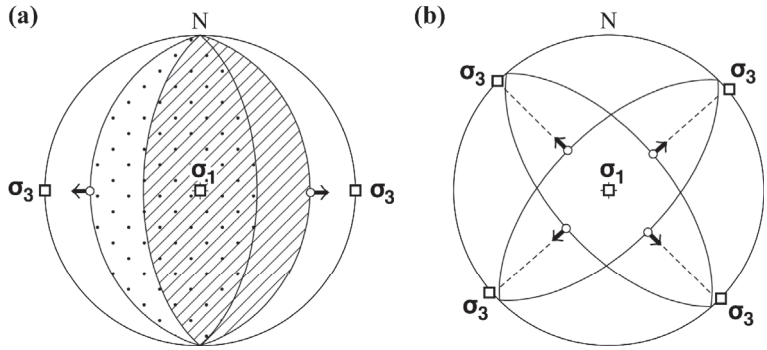

Figure 11.8: Schematic illustrations showing the ambiguity of stresses inferred from fault-slip data. (a) Conjugated dip-slip normal faults and the principal orientations (squares) of the stress that formed the faults. Dotted and hatched regions designate the σ_1 orientations compatible with the west- and east-dipping normal faults, respectively. These regions correspond to the solid region in Fig. 11.7. (b) Two sets of conjugated dip-slip normal faults. The sets were formed successively by NE–SW and NW–SE extensional stresses. Both stereograms are lower-hemisphere equal-angle projections.

11.3 Stress inversion

It is possible to determine the state of stress from fault-slip data. The tangent-lineation diagram in Fig. 11.6 shows a set of natural data collected from mesoscale faults in mid-Quaternary sedimentary rocks in central Japan. Obviously, many arrows in the diagram are directed along a WNW–ESE orientation, suggesting that the faults corresponding to the arrows were activated by WNW–ESE trending extensional stress.

This inference is mathematically formulated as the following inverse method, by which the optimal state of stress is determined from given fault-slip data [6, 7, 190]. Assuming the principal stress orientations and a stress ratio, we compose a stress tensor $\boldsymbol{\sigma}_0$ using Eq. (11.8). Secondly, the theoretical slip direction is calculated by Eq. (11.3) for each fault. Thirdly, let $\Delta^{(i)}$ be the angular misfit between the theoretical and observed slip directions of the ith fault. As we assumed the principal orientations and stress ratio to be arbitral, it is natural that the directions are not parallel. Then, the sum

$$S = \sum_{i=1}^{N} f(\Delta^{(i)}) \tag{11.9}$$

can be used as the measure of misfit of the assumed stress state to the data set, where N is the number of faults and $f(\,)$ is a monotonously decreasing function such as that shown in Fig. 11.9. S is a function of not only the data but also of the principal orientations and stress ratio. Accordingly, the optimal state of stress is determined by maximizing $S(\boldsymbol{\sigma}_0)$. In inverse theory, this is called an

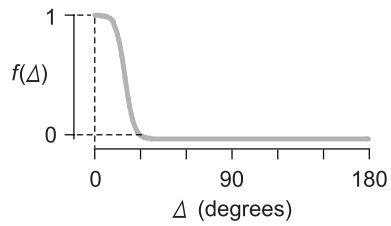

Figure 11.9: Graph of a monotonously decreasing function $f(\Delta)$ used in stress inversion.

object function.

This method is referred to as stress inversion[4]. Contrasting with the recent numerical techniques that are introduced in the next section, this is sometimes called the classical inverse method. The stress inversion is a non-linear inverse method, because the slip direction is denoted by the unit vector $-\boldsymbol{\sigma}_S/|\boldsymbol{\sigma}_S|$. The non-linearity comes from this division [150].

The optimal stress determined by the stress inversion has uncertainty resulting from the independence of the slip direction from p and q in Eq. (11.7). The absolute values of stress components are not known. Instead, the tensor defined by Eq. (11.8) is determined, i.e., the optimal principal orientations and the optimal stress ratio are obtained by the inverse method.

Figure 11.10 shows the optimal stress determined through the stress inversion for the natural data in Fig. 11.6. The result is a WNW–ESE trending extensional stress, which coincides with the stress roughly inferred by eye from the tangent-lineation diagram of the data.

However, the optimal solution is not satisfactory as the histogram of angular misfits is definitely bimodal. About two-fifths of the faults have misfits greater than 60°. The optimal stress cannot explain the observed slip directions of those faults, indicating that the fault-slip data are heterogeneous. Fault-slip data is called heterogeneous if plural stress states were responsible for the faults. Consequently, the forearc region in central Japan experienced a polyphase stress history since the Otadai Formation, from which the data were obtained, deposited in the mid Quaternary [151].

Given heterogeneous fault-slip data the object function $S(\boldsymbol{\sigma}_0)$ has maxima, and the optimal solution might be a meaningless solution [265]. Thus, we have to input homogeneous fault-slip data for the calculation. For this purpose, researchers try to sort faults at outcrops by their apparent ages.

There are several criteria [10, 39, 250]. The principal guides for distinguishing the different fault sets are (1) consideration of stratigraphy or of the age of the rocks affected by a certain deformation, (2) characterization of the synsedimentary faults such as fault drag, (3) cross-cutting relationships, (4) superimposed striae on the same fault plane and (5) association of mineral veins. Unfortunately, these criteria are not always available in the field, especially in young geologic units such as the mid-Quaternary Otadai Formation. In addition, the resemblance of the orientation of fault planes and slip directions is sometimes employed for fault sorting. However, many faults with the same orientations

[4]See [9] for further reading.

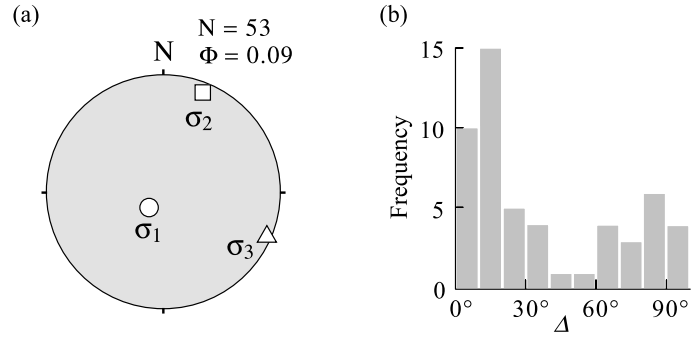

Figure 11.10: (a) Lower-hemisphere stereonet showing the optimal stress determined from the data shown in Fig. 11.6 via the classical inverse method. The number of data is $N = 53$. The σ_1- and σ_3-axes are nearly vertical and horizontal so that this is a normal faulting regime of stress. The optimal stress ratio is $\Phi = 0.09$ so that the optimal stress is approximately of axial compression. (b) Histogram showing the angular misfits for the optimal stress illustrated in the left stereonet.

and the same slip directions can be activated by different stresses (Fig. 11.7). Therefore, such fault classification implicitly restricts solutions prior to using the stress inversion.

Researchers have tackled the problem how to separate stresses from heterogeneous fault slip data, and several numerical techniques have been proposed. Before explaining one of the techniques in Section 11.5, we will introduce an other formulation of the classical stress inversion in the next section.

11.4 Fry's formulation of stress inversion

The classical stress inversion is a non-linear inverse method [150]. Fry (1999) [60] divided the inversion into linear and non-linear parts as follows.

Given a fault-slip datum, a unit vector $\boldsymbol{b}$ on the fault plane is defined perpendicular to the observed slip direction, i.e., $\boldsymbol{b}$ is the null vector [80]. The vector is parallel to the line OB in Fig. 11.4. If the theoretical slip direction is parallel to the observed one, the traction vector upon the fault plane should lie on the M-plane. Therefore, $\boldsymbol{b}$ should be perpendicular to the traction vector $\boldsymbol{t}(\boldsymbol{n})$, i.e., $\boldsymbol{b} \cdot (\boldsymbol{\sigma} \cdot \boldsymbol{n}) = 0$. This is rewritten using components of these vectors and tensors as

$$\sum_{i,j=1}^{3} b_i \sigma_{ij} n_j = 0. \tag{11.10}$$

The symmetry of $\boldsymbol{\sigma}$ allows us to rewrite the left-hand side of this equation as

$$\sum_{i,j=1}^{3} \sigma_{ij} b_i n_j = \sum_{i,j=1}^{3} \sigma_{ji} b_i n_j = \sum_{i,j=1}^{3} \sigma_{ij} b_j n_i. \tag{11.11}$$

In the last transformation, the dummy indices i and j are exchanged. Consequently, Eq. (11.10) is rewritten as

$$\sum_{i,j=1}^{3} b_j \sigma_{ij} n_i = 0. \tag{11.12}$$

Adding both sides of Eqs. (11.10) and (11.12) gives[5]

$$\sum_{i,j=1}^{3} \sigma_{ij} f_{ij} = 0, \tag{11.13}$$

where

$$f_{ij} = b_i n_j + b_j n_i.$$

Note that $\boldsymbol{n}$ and $\boldsymbol{b}$ are observable quantities but $\boldsymbol{\sigma}$ is unknown. Accordingly, we can compose the tensor f_{ij} from the fault-slip datum. In addition, f_{ij} has six degrees of freedom, because of the symmetry $f_{ij} = f_{ji}$. Therefore, Eq. (11.13) is further rewritten as the scalar product

$$\boldsymbol{s} \cdot \boldsymbol{f} = 0, \tag{11.14}$$

where $\boldsymbol{s} = (\sigma_{11},\ \sigma_{12},\ \sigma_{13},\ \sigma_{22},\ \sigma_{23},\ \sigma_{33})^{\mathrm{T}}$ and $\boldsymbol{f} = (f_{11},\ f_{12},\ f_{13},\ f_{22},\ f_{23},\ f_{33})^{\mathrm{T}}$. The components of these vectors are independent components of the tensors σ_{ij} and f_{ij}.

Equation (11.14) indicates that the vectors $\boldsymbol{s}$ and $\boldsymbol{f}$ meet at right-angles in six-dimensional space if the assumed stress $\boldsymbol{\sigma}$ fits the fault-slip datum. If $|\boldsymbol{s} \cdot \boldsymbol{f}|$ does not vanish, $\boldsymbol{\sigma}$ is not appropriate for the datum. Accordingly, we define the unit vector $\overline{\boldsymbol{f}} = \boldsymbol{f}/|\boldsymbol{f}|$ so that the endpoint of the position vector $\overline{\boldsymbol{f}}$ is represented by a point on the six-dimensional unit sphere.

Let $\boldsymbol{f}^{(k)}$ be the unit vector for the kth datum. If the stress is compatible with all the fault-slip data, then the stress tensor must satisfy the equation

$$\sum_{k=1}^{N} \boldsymbol{s} \cdot \boldsymbol{f}^{(k)} = 0. \tag{11.15}$$

This equation has the geometrical interpretation that the end points of the unit vectors, $\overline{\boldsymbol{f}}^{(1)}, \ldots, \overline{\boldsymbol{f}}^{(N)}$, are on the great circle whose pole is parallel to the vector $\boldsymbol{s}$. The scalar product $\boldsymbol{s} \cdot \boldsymbol{f}$ becomes negative in sign if the angle between the two vectors is greater than 90°. Therefore, the stress inversion can be reformulated as the least-squares method to minimize the quantity

$$\sum_{k=1}^{N} \left[\boldsymbol{s} \cdot \boldsymbol{f}^{(k)}\right]^2.$$

[5]Comparing the following equation with Eqs. (2.49) and (2.54) in Section 2.7, it is seen that Eq. (11.13) indicates that the work done by the shear traction in the orientation perpendicular to the observed slip direction is nil.

This is equivalent withto

$$\sum_{k=1}^{N}\left[\sum_{i=1}^{6} s_i f_i^{(k)}\right]\left[\sum_{j=1}^{6} s_j f_j^{(k)}\right] = \sum_{k=1}^{N}\sum_{i,j=1}^{6} s_i f_i^{(k)} f_j^{(k)} s_j = \sum_{i,j=1}^{6} s_i \left[\sum_{k=1}^{N} f_i^{(k)} f_j^{(k)}\right] s_j = \boldsymbol{s}\cdot\boldsymbol{g}\cdot\boldsymbol{s},$$

where

$$\boldsymbol{g} = \left(\sum_{k=1}^{N} f_i^{(k)} f_j^{(k)}\right)$$

is a six-dimensional, second-order, symmetric tensor, and is composed from given fault-slip data.

The optimal stress determined by the stress inversion has uncertainty resulting from the independence of the slip direction from p and q in Eq. (11.7). The absolute values of the stress components are not known. Accordingly, the uncertainty allows us to assume $\boldsymbol{s}$ to be a unit vector.

The least-squares method that we should solve is to search the optimal vector $\boldsymbol{s}$ that minimizes the quadratic form $\boldsymbol{s}\cdot\boldsymbol{g}\cdot\boldsymbol{s}$ with the constraint $\boldsymbol{s}\cdot\boldsymbol{s} = 1$. The constraint designate that the end point of the vector is on the six-dimensional unit sphere. This extreme value problem is solved through Lagrange's method of the undetermined multiplier, i.e., we seek the extremal of the function,

$$\mathcal{L} = \boldsymbol{s}\cdot\boldsymbol{g}\cdot\boldsymbol{s} - \lambda(\boldsymbol{s}\cdot\boldsymbol{s} - 1) = 2\boldsymbol{s}\cdot(\boldsymbol{g} - \lambda\boldsymbol{I})\cdot\boldsymbol{s} - \lambda,$$

where λ is the Lagrange multiplier. Since the tensor $(\boldsymbol{g} - \lambda\boldsymbol{I})$ is symmetric, the formula in Eq. (C.61) applies to this tensor, and we obtain

$$\frac{\partial\mathcal{L}}{\partial\boldsymbol{s}} = 2(\boldsymbol{g}\cdot\boldsymbol{s} - \lambda\boldsymbol{s}) = 0.$$

Consequently, we obtain the characteristic equation,

$$\boldsymbol{g}\cdot\boldsymbol{s} = \lambda\boldsymbol{s}. \tag{11.16}$$

A symmetric tensor has real eigenvalues. Therefore, all the roots of this equation are real. We are seeking the eigenvector $\boldsymbol{s}$ that minimizes $\mathcal{L}$. Noticing $\boldsymbol{s}\cdot\boldsymbol{s} = 1$, we obtain $\boldsymbol{s}\cdot\boldsymbol{g}\cdot\boldsymbol{s} = \boldsymbol{s}\cdot\lambda\boldsymbol{s} = \lambda$ from Eq. (11.16). The left-hand side of this equation equals $\mathcal{L}$ so that the minimum absolute eigenvalue corresponds to the minimum $\mathcal{L}$, and the corresponding eigenvector gives the optimal stress [209].

It was shown that the optimal vector $\boldsymbol{s}$ is parallel to the pole to the great circle along which the endpoints of the data vectors $\overline{\boldsymbol{f}}^{(1)}, \ldots, \overline{\boldsymbol{f}}^{(N)}$ are aligned. Fitting of a great circle to the data vectors is a eigenproblem to solve Eq. (11.16). This is a linear inverse problem.

Once a great circle is fitted, we have two poles for that circle. If one of the poles is represented by $\boldsymbol{s}$, the other is $-\boldsymbol{s}$. These vectors correspond to the stresses $\boldsymbol{\sigma}$ and $-\boldsymbol{\sigma}$. Therefore, we have to choose one of them. The slip directions corresponding to the stresses are given by $-\boldsymbol{\sigma}_S = \pm(\boldsymbol{N} - \boldsymbol{I})\cdot\boldsymbol{\sigma}\cdot\boldsymbol{n}$ (Eq. (11.3)). That is, the stresses causes the opposite sense of movement for entire faults so that we can choose one of the stresses corresponding to the correct sense of movement. The choice of the correct pole is a non-linear operation. The stress inversion is, therefore, divided into linear and non-linear parts[6].

[6] See Appendix B and [203, 269].

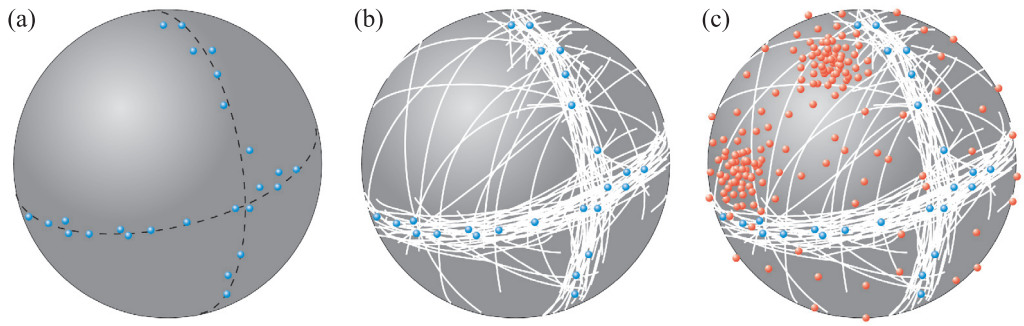

Figure 11.11: Schematic illustrations showing the principle of the multiple inverse method. (a) Data points are aligned on two great circles (dotted lines) on the six-dimensional unit sphere. (b) White arcs showing parts of the great circles that are fitted to k-element subsets of the data points, where k generally equals 5. (c) The poles of the great circles are plotted to exhibit the optimal stress for the subsets. The poles make clusters at the poles for the great circles indicated by the dotted lines in (a).

11.5 Multiple inverse method

The purpose of this section is to explain the multiple inverse method, a numerical technique used for separating stresses from heterogeneous fault-slip data [264].

11.5.1 Principle

It was shown in the previous section that the stress inversion is compared to fitting a great circle to data points on the six-dimensional unit sphere, and that one of the poles of the great circle represents the optimal stress. Therefore, heterogeneous fault-slip data are represented by data points that are aligned on plural great circles on the unit sphere. Suppose that a set of observed faults is a mixture of two assemblages that were activated by two different stresses. Then, the fault-slip data are represented by two great circles on the unit sphere (Fig. 11.11(a)). Consequently, it is the problem how to identify the great circles. The basic idea of the method is that the generalized Hough transform is applicable to this problem. The transform is a technique of artificial intelligence to detect objects with arbitrary shapes and orientations [31]. The objects in our problem are stress ellipsoids with different shapes and different orientations.

The method firstly constructs k-element subsets from the entire fault-slip data. Given N faults, we have ${}_N\mathrm{C}_k$ subsets, where

$$ {}_N\mathrm{C}_k = \frac{N!}{k!(N-k)!} $$

is the binomial coefficient. Secondly, great circles are fitted to the subsets[7]. Thirdly, the poles of the great circles that represent the optimal stresses for the subsets are plotted on the unit sphere. There

[7] It was shown that the resolution of this method is greatly improved by choosing a particular kind of subsets [168].

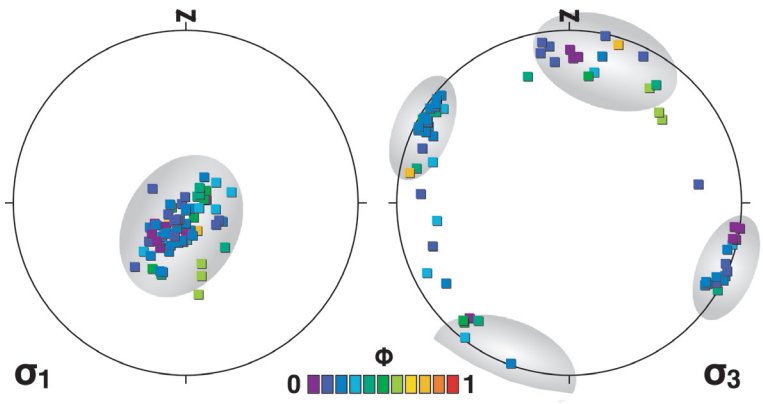

Figure 11.12: Left and right stereograms (lower-hemisphere equal-area projection) showing the σ_1- and σ_3-orientations, respectively, of the optimal stresses determined by the multiple inverse method with $k = 5$ applied to the fault-slip data shown in Fig. 11.6. Stress ratios are indicated by different colors. Clusters (shaded) indicates that WNW–ESE and NNE–SSW trending extensional stresses affected the faulting in the Otadai Formation.

are eventually two clusters of the poles to the two great circles. The clusters are expected to appear at the correct positions if the data points are plotted within narrow belts along the two great circles, as most of the great circles fitted to the k-element subsets are nearly parallel to either of the two great circles (Fig. 11.11(b)). However, if the belts are wide or the number of data points is small, the density of the clusters decreases. The density designates the statistical significance of the stresses represented by the clusters.

Tthe final task is to detect the clusters. For this purpose, the optimal stresses are mapped onto a stereogram. The stress ratios of the optimal stresses are depicted by colors. Figure 11.12 shows an example, where WNW–ESE and NNE–SSW trending extensional stresses are detected from the fault-slip data exhibited in Fig. 11.6. The former is represented by the cluster of blue squares in Fig. 11.12, and the color indicates $\Phi \approx 0.1$. Therefore, the classical inverse method detected the WNW–ESE extension (Fig. 11.10).

11.5.2 Average and spread of clusters

The right stereogram in Fig. 11.6 demonstrates that the density and spread of the clusters indicate the WNW–ESE extension is statistically more significant than the NNE–SSW extension. The spread of a cluster is quantified as follows.

Firstly, we introduce the *stress difference*, a parameter to quantify the difference between two stress states [164]. The uncertainty related to p and q in Eq. (11.7) demonstrates that the mean and differential stresses are indeterminable for the stress inversion. In addition, the definition of

a reduced stress tensor is not unique. Accordingly, we define the reduced stress tensor $\overline{\boldsymbol{\sigma}}$ so as to satisfy the two conditions

$$\text{trace}\,\overline{\boldsymbol{\sigma}} = \overline{\sigma}_{11} + \overline{\sigma}_{22} + \overline{\sigma}_{33} = 0 \tag{11.17}$$

and the octahedral shear stress of unity. Equation (11.17) indicates that $\overline{\boldsymbol{\sigma}}$ is a deviatoric tensor so that the second basic invariant of this tensor is given by Eq. (4.13). Following Eq. (4.17), we have the second condition as

$$\frac{1}{3}\left(\overline{\sigma}_{11}^2 + \overline{\sigma}_{22}^2 + \overline{\sigma}_{33}^2 + 2\overline{\sigma}_{12}^2 + 2\overline{\sigma}_{23}^2 + 2\overline{\sigma}_{31}^2\right) = 1. \tag{11.18}$$

Using the reduced stress, we have the stress tensor $\boldsymbol{R}\cdot\overline{\boldsymbol{\sigma}}\cdot\boldsymbol{R}^{\mathrm{T}}$ for the stress tensor inversion.

Secondly, given two reduced stress tensors, $\overline{\boldsymbol{\sigma}}^{(1)}$ and $\overline{\boldsymbol{\sigma}}^{(2)}$, the difference between the stress states represented by the tensors is defined by the octahedral shear stress of the tensor $\boldsymbol{\Delta} = \overline{\boldsymbol{\sigma}}^{(1)} - \overline{\boldsymbol{\sigma}}^{(2)}$. Namely, the difference is given by

$$D = \frac{1}{3}\sqrt{(\Delta_{11}-\Delta_{22})^2 + (\Delta_{22}-\Delta_{33})^2 + (\Delta_{33}-\Delta_{11})^2 + 6\,(\Delta_{12})^2 + 6\,(\Delta_{23})^2 + 6\,(\Delta_{31})^2}. \tag{11.19}$$

Orife and Lisle [164] term this parameter "stress difference", and demonstrate that D is in the range between 0 and 2 for any combination of reduced stress tensors provided that they satisfy the conditions indicated by Eqs. (11.17) and (11.18). The similarlity between two reduced stress tensors is indicated by $(2 - D)$. If $D = 0$, the two stress states result in the same slip directions whatever the orientations of faults are. If $D = 2$, the two stress states cause faulting with the opposite slip directions. The couple of stresses with $D = 2$ are called inverse stresses.

Finally, the spread of stress states is defined as follows. Given m reduced stress tensors, $\overline{\boldsymbol{\sigma}}^{(1)}, \ldots, \overline{\boldsymbol{\sigma}}^{(m)}$, their average is defined by

$$\langle\overline{\boldsymbol{\sigma}}\rangle = \frac{1}{m}\left[\overline{\boldsymbol{\sigma}}^{(1)} + \cdots + \overline{\boldsymbol{\sigma}}^{(m)}\right]. \tag{11.20}$$

The average principal orientations are obtained as the eigenvectors of this tensor, and the average stress ratio is given by the equation

$$\langle\Phi\rangle = \frac{\langle\sigma\rangle_2 - \langle\sigma\rangle_3}{\langle\sigma\rangle_1 - \langle\sigma\rangle_3},$$

where $\langle\sigma\rangle_i$ is the ith largest eigenvalue of the tensor $\langle\overline{\boldsymbol{\sigma}}\rangle$. The spread of the reduced stress tensors around the average is defined by the average stress difference

$$\langle D\rangle = \frac{1}{m}\left[D^{(1)} + \cdots + D^{(m)}\right], \tag{11.21}$$

where $D^{(i)}$ is the stress difference between $\overline{\boldsymbol{\sigma}}^{(i)}$ and the reduced stress tensor derived $\langle\boldsymbol{\sigma}\rangle$. The greater the scatter of the stress states the larger the average stress difference. Therefore, $\langle D\rangle$ is a measure of the spread of stress states[8].

[8]he average of the values of $2\sin^{-1}(D/2)$ is more useful than that of D values. See Appendix B.

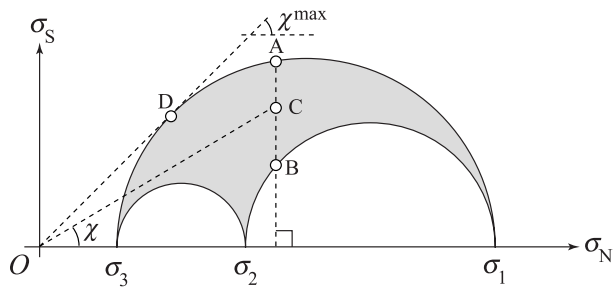

Figure 11.13: Mohr circles for a triaxial stress and the slope tan χ.

The multiple inverse method yields clusters of stress states, and the center and spread of a cluster are evaluated by Eqs. (11.20) and (11.21). The identification of those clusters can be computerized using the k-means algorithm [167], a technique of artificial intelligence [52], with the average and spread of the clusters.

It is difficult to apply stress inversion to fold belts as the timing of faulting relative to folding is difficult to know. Therefore, it is sometimes assumed a-priori that a reverse faulting regime of stress accompanied folding.

The bedding tilt test used in paleomagnetism can be applied to this problem using the multiple inverse method and the average and spread of clusters [270]. Paleomagnetists uses the statistic α_{95} to evaluate the spread of paleomagnetic vectors determined at various parts of a fold [32]. The larger the statistic, the more the vectors are scattered. If rocks in the fold acquired the paleomagnetism before folding, untilting of the vectors makes α_{95} smaller. If, on the other hand, the rocks were magnetized after folding, the statistic becomes larger by the untilting. Therefore, the statistic works as an object function to be minimized in the inverse problem to determine the optimal timing magnetization relative to folding.

Similarly, we are able to use $\langle D \rangle$ instead of α_{95} to be minimized in the inverse problem for determining the optimal timing of faulting relative to folding. This test procedure was applied to mesoscale faults in a Quaternary fold in central Japan and revealed that the majority of the faults were activated by a strike-slip faulting regime of stress at the middle of folding [270].

11.6 Slip tendency

The Wallace-Bott hypothesis concerns the fact that any faults can be activated, unless the fault plane is one of the principal planes of stress. Shear stress on the plane vanishes so that those faults cannot move. However, if fault planes have the same coefficient of friction, faults nearly parallel to the principal plane may be difficult to move compared to those oblique to the principal planes. The magnitude of shear stress is depicted by the Mohr diagram (Figs. 4.6 and 11.13).

Slip tendency [157] is a yardstick for the mobility of fault surfaces under a given stress $\boldsymbol{\sigma}$. The

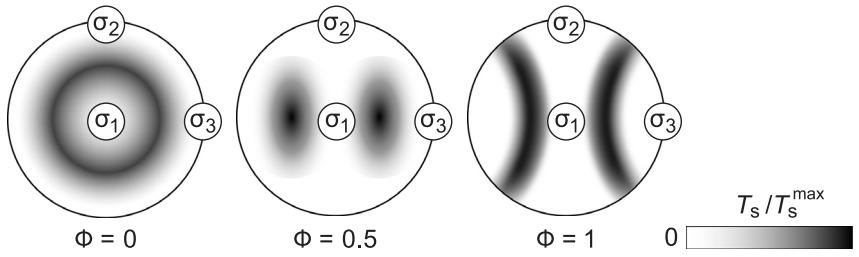

Figure 11.14: Stereonets showing slip tendency T_s for three stresses with the same principal orientations (open circles) but with different stress ratios, $\Phi = 0$, 0.5 and 1.

frictional resistance of the fault with the unit normal $\boldsymbol{n}$ is $\mu_f \sigma_N = \mu_f(\boldsymbol{n} \cdot \boldsymbol{\sigma} \cdot \boldsymbol{n})$. A fault is thought to be preferable for $\boldsymbol{\sigma}$ if the shear stress on the fault, $\sigma_S = |(\boldsymbol{I} - \boldsymbol{N}) \cdot \boldsymbol{\sigma} \cdot \boldsymbol{n}|$, is much large compared with F_s, i.e., the slip tendency is defined as

$$T_s \equiv \left| \frac{\sigma_S}{\mu_f \sigma_N} \right| = \frac{1}{\mu_f} \left| \frac{(\boldsymbol{I} - \boldsymbol{N}) \cdot \boldsymbol{\sigma} \cdot \boldsymbol{n}}{\boldsymbol{n} \cdot \boldsymbol{\sigma} \cdot \boldsymbol{n}} \right| .$$

T_s is a function of $\boldsymbol{n}$, $\boldsymbol{\sigma}$ and μ_f. Given $\boldsymbol{\sigma}$ and μ_f, T_s has the maximum T_s^{max} for the fault orientations.

For simplicity, we assume that all faults have the same coefficient of friction to investigate the relationship of the mobility with fault orientations. Then, the angle χ shown in Fig. 11.13 is related to the slip tendency as $\tan \chi = T_s$. The points A, B and C have a common normal stress but different shear stresses. The points A and B have maximum and minimum χs, respectively. It is obvious that the fault plane designated by point D has the maximum χ, because the line OD is tangent to the outer Mohr circle. However, the Mohr diagram is not convenient to see how the slip tendency changes with different orientations.

Therefore, the ratio T_s/T_s^{max} is a convenient measure to consider the orientation-dependence of the slip tendency. The variation of this ratio is shown by the gray scales in Fig. 11.14. The central panel in this figure illustrates the relationship between the slip tendency and fault orientations for triaxial stresses. There are two dark spots in the stereogram, demonstrating that the fault surfaces parallel to the σ_2-axis and making an acute angle with σ_1-axis have a maximum slip tendency under triaxial stresses. The two spots represent conjugate faults. The slip tendency has a orthorhombic symmetry with respect to the principal planes of stress.

In contrast, the slip tendency for axial compression and axial tension has axial symmetry with respect to the σ_1- and σ_3-axes, respectively (Fig. 11.14). The planes tangent to a cone whose axis is parallel to the symmetry axis of stress are referentially activated as faults [95].

In reality, every fault may have its own coefficient of friction, and pore pressure may be different for each faulting event. Accordingly, the slip tendency is not the only factor to indicate the mobility. However, Fig. 11.14 helps in considering fault activity under a specified state of stress.

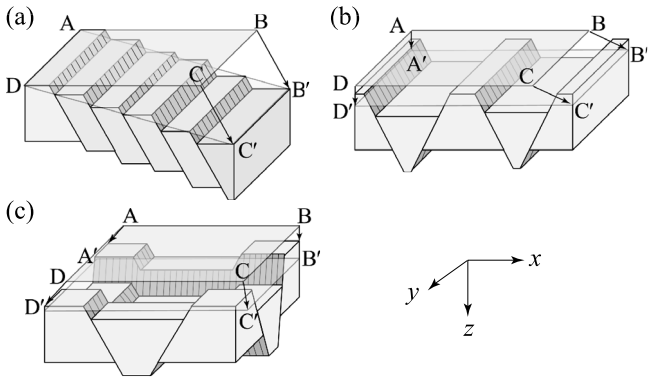

Figure 11.15: Strain of a rock mass by the activity of fault sets in the mass, where faults belonging to a set have similar fault orientations and slip directions. Rectangle ABCD indicates the initial top surface of the mass. The z-axis is defined as being vertically downward. Although displacement is shown along two or several faults for each set, the parallel faults carry similar displacements. (a) The activity of a set of normal faults parallel to the y-axis and slip direction normal to the y-axis, the mass suffers a plane strain on the xz-plane. The points B and C are transferred to B′ and C′ by the faulting, resulting in an inclined top surface AB′C′D. (b) Two sets of faults making up conjugated normal faults. If the total displacements of each set are equal to each other, the top surface remains horizontal only to subside to the rectangle A′B′C′D′. The deformation of the mass is approximated by a pure shear. (c) Four sets of faults leading to a three-dimensional coaxial deformation, i.e., the top surface is kept horizontal.

11.7 Faulting controlled by strain

A rock mass encompassing faults deforms by the fault activity (Fig. 1.17). If there are a lot of faults with much smaller displacements than the size of the mass, the deformation can be regarded as a continuous plastic deformation.

Faulting obeying Anderson's theory leads only to a plane strain (Exercise 11.1). However, strains may be generally three-dimensional. The faulting predicted by the Wallace-Bott hypothesis allows three-dimensional strains. When we used the hypothesis, stress was assumed to control faulting. However, stress is not observable. We observe the strain of a rock mass through faults, and the hypothesis transforms strain into stress. In contrast, what would happen if strain controls faulting? The present and next sections deal with this problem.

Natural faults often form groups with similar orientations and slip directions. Here, we sort faults by the orientations and directions into sets of faults (Fig. 11.15). One region may have multiple sets of faults, which may or may not have been activated at the same time.

For simplicity, we assume that all faults belonging to a set have the same displacements and that they are uniformly distributed in the rock mass. Then, the deformation of the mass due to internal fault activity can be regarded as a uniform deformation. The deformation by a single set of faults

equals an infinitesimal simple shear in the M-plane of the faults. The top surface ABCE in Fig. 11.15(a) is transformed into the inclined rectangle AB′C′D by this simple shear unless the fault planes are horizontal. Two sets of faults enable pure shears that keep the top surface horizontal (Fig. 11.15(b)). If there are four sets of faults, coaxial deformations are possible (Fig. 11.15(c)).

Not only coaxial but also any three-dimensional deformations are possible if there are at least four fault sets [193]. Here, faulting is assumed not to accompany any volume change of the rock mass, so that we have $|\boldsymbol{F}| = 1$, where $\boldsymbol{F}$ is the deformation gradient of the rock mass. $\boldsymbol{F}$ has nine independent components in three dimensions. However, the volume conservation reduces the degrees of freedom of $\boldsymbol{F}$ to eight. One set has two degrees of freedom, the rake of slip direction on the fault planes and the parameter q of the simple shear (Eq. (1.13)), if the orientations of fault planes are given. Therefore, four fault sets are sufficient to accommodate a general incompressive deformation in three dimensions.

If a three-dimensional deformation controls faulting, at least a few sets of faults should be activated to accommodate the deformation. Fault systems comprised of four fault sets are often observed in the field and in clay cake experiments [131, 163, 193, 195].

11.8 Reches' model

We now consider faulting controlled by a prescribed strain of a rock mass that includes the faults. Reches [193, 194] applied a classical theory of the plastic deformation of single crystals. The plastic deformation is due to the movement of dislocations through the crystal lattice. The lattice structure allows a limited number of slip systems whose glide planes and slip directions are constrained. For example, a face-centered cubic lattice has 12 slip systems. Minimizing energy dissipation, Taylor (1938) linked the slippage on the planes with the macroscopic deformation of the crystal containing the slip systems [239]. Unlike single crystals, a rock mass has numberless planes of fractures with various orientations that are capable of faulting. However, the following argument reduces the possible number of fault sets to four.

It is assumed that there are numberless pre-existing fractures capable of accommodating an applied three-dimensional coaxial strain, but that most preferable surfaces are activated. The rock mass is also assumed to be homogeneous and isotropic in the broad view so that the stress and strain have the same principal orientations. Since the controlling factor is the coaxial strain that has an orthorhombic symmetry about the principal planes of strain, the resultant faulting may have the same symmetry, i.e., the four sets of faults the orientations of which are arranged symmetrically with respect to the planes (Fig. 11.16(a)). Four sets are necessary and sufficient to accommodate the prescribed strain of the rock mass. To keep the symmetry, they carry the same magnitude of strain. Here, they are called *orthorhombic fault sets*.

Each fault set has many faults but the displacements are very small compared to the dimension of the rock mass. In addition, faults belonging to a set are located with constant intervals. Therefore, the deformation of the mass is regarded as continuous and homogeneous. Let the unit vectors $\boldsymbol{n}^{(i)} =$

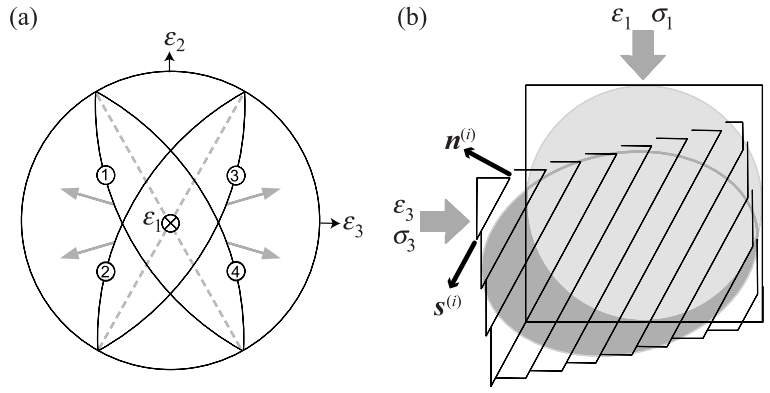

Figure 11.16: (a) Orthorhombic fault sets arranged symmetrical with respect to the principal planes of stress. Equal-angle projection. The rectangular Cartesian coordinates O-123 are defined as being parallel to the principal axes of strain. The O-1 axis is directed out of the page. Ordinal numbers of the fault sets are encircled. Gray arrows points the slip directions. (b) The rock mass encompassing the fault sets is assumed to suffer a coaxial deformation by the slippage on the faults, each of which carries a simple shear. The unit vectors $\boldsymbol{n}^{(i)}$ and $\boldsymbol{s}^{(i)}$ represent the pole to the fault planes and slip direction of the ith set, respectively.

$\left(n_1^{(i)},\, n_2^{(i)},\, n_3^{(i)}\right)^{\mathrm{T}}$ and $\boldsymbol{s}^{(i)} = \left(s_1^{(i)},\, s_2^{(i)},\, s_3^{(i)}\right)^{\mathrm{T}}$ be the unit normal and slip direction of the ith fault set (Fig. 11.16(b)), where the coordinates O-123 are defined parallel to the principal axes of stress of the rock mass (Fig. 11.16(a)). From the orthorhombic symmetry, we have

$$\boldsymbol{n}^{(1)} = \begin{pmatrix} n_1 \\ n_2 \\ n_3 \end{pmatrix}, \quad \boldsymbol{n}^{(2)} = \begin{pmatrix} n_1 \\ -n_2 \\ n_3 \end{pmatrix}, \quad \boldsymbol{n}^{(3)} = \begin{pmatrix} -n_1 \\ -n_2 \\ n_3 \end{pmatrix}, \quad \boldsymbol{n}^{(4)} = \begin{pmatrix} -n_1 \\ n_2 \\ n_3 \end{pmatrix} \tag{11.22}$$

and

$$\boldsymbol{s}^{(1)} = \begin{pmatrix} s_1 \\ s_2 \\ s_3 \end{pmatrix}, \quad \boldsymbol{s}^{(2)} = \begin{pmatrix} s_1 \\ -s_2 \\ s_3 \end{pmatrix}, \quad \boldsymbol{s}^{(3)} = \begin{pmatrix} -s_1 \\ -s_2 \\ s_3 \end{pmatrix}, \quad \boldsymbol{s}^{(4)} = \begin{pmatrix} -s_1 \\ s_2 \\ s_3 \end{pmatrix}, \tag{11.23}$$

where $0 \leq n_1,\, n_2,\, n_3$. The hypothesis of orthorhombic fault sets results in a tight constraint between $\boldsymbol{n}$ and $\boldsymbol{s}$.

Suppose the rock mass has M faults. Let $\boldsymbol{f}^{(i)} = \boldsymbol{I} + \delta\boldsymbol{f}^{(i)}$ be the deformation gradient due to the ith fault, where i represents the sequence of faulting. Then the total strain of the rock mass is given by the multiplication $\boldsymbol{F} = \boldsymbol{f}^{(M)} \cdots \boldsymbol{f}^{(1)} = \left[\boldsymbol{I} + \delta\boldsymbol{f}^{(M)}\right] \cdots \left[\boldsymbol{I} + \delta\boldsymbol{f}^{(1)}\right] \approx \boldsymbol{I} + \boldsymbol{f}^{(M)} + \cdots + \boldsymbol{f}^{(1)}$, where second-order terms are neglected. Since the addition of matrices is commutative, the total strain is independent from the order of fault activity. Therefore, we define $\boldsymbol{F}^{(i)} = \boldsymbol{I} + \delta\boldsymbol{F}^{(i)}$ as the deformation gradient due to the faults belonging to the ith fault set, when we have the deviation of the total strain from $\boldsymbol{I}$,

$$\delta\boldsymbol{F} = \delta\boldsymbol{F}^{(1)} + \delta\boldsymbol{F}^{(2)} + \delta\boldsymbol{F}^{(3)} + \delta\boldsymbol{F}^{(3)}. \tag{11.24}$$

Comparing Eqs. (2.53) and (11.24), we have

$$\delta \boldsymbol{F}^{(i)} = \gamma^{(i)} \boldsymbol{s}^{(i)} \boldsymbol{n}^{(i)}, \tag{11.25}$$

where $\gamma^{(i)}$ represents the contribution of the ith set to the total strain. $\boldsymbol{F}^{(i)}$ represents an infinitesimal simple shear. Therefore, taking a proper coordinate system, we have also the following expression (Eq. (1.13)):

$$\boldsymbol{F}^{(i)} = \begin{pmatrix} 1 & 2q^{(i)} & 0 \\ 0 & 1 & 0 \\ 0 & 0 & 1 \end{pmatrix} \quad \therefore \quad \delta \boldsymbol{F}^{(i)} = \begin{pmatrix} 0 & 2q^{(i)} & 0 \\ 0 & 0 & 0 \\ 0 & 0 & 0 \end{pmatrix}.$$

Since q in these matrices represents the infinitesimal shear strain that is half of the engineering shear strain (p. 34), $\gamma^{(i)}$ in Eq. (11.25) represents the engineering shear strain for the ith set. The orthorhombic symmetry requires

$$\gamma \equiv \gamma^{(1)} = \gamma^{(2)} = \gamma^{(3)} = \gamma^{(4)}. \tag{11.26}$$

Combining Eqs. (11.22)–(11.26), we obtain the total deformation

$$\begin{aligned} \delta \boldsymbol{F} = {} & \gamma \begin{pmatrix} n_1 s_1 & n_2 s_1 & n_3 s_1 \\ n_1 s_2 & n_2 s_2 & n_3 s_2 \\ n_1 s_3 & n_2 s_3 & n_3 s_3 \end{pmatrix} + \gamma \begin{pmatrix} n_1 s_1 & -n_2 s_1 & n_3 s_1 \\ -n_1 s_2 & n_2 s_2 & -n_3 s_2 \\ n_1 s_3 & -n_2 s_3 & n_3 s_3 \end{pmatrix} \\ & + \gamma \begin{pmatrix} n_1 s_1 & n_2 s_1 & -n_3 s_1 \\ n_1 s_2 & n_2 s_2 & -n_3 s_2 \\ -n_1 s_3 & -n_2 s_3 & n_3 s_3 \end{pmatrix} + \gamma \begin{pmatrix} n_1 s_1 & -n_2 s_1 & -n_3 s_1 \\ -n_1 s_2 & n_2 s_2 & n_3 s_2 \\ -n_1 s_3 & n_2 s_3 & n_3 s_3 \end{pmatrix} = 4\gamma \begin{pmatrix} n_1 s_1 & 0 & 0 \\ 0 & n_2 s_2 & 0 \\ 0 & 0 & n_3 s_3 \end{pmatrix}. \end{aligned}$$

Hence, the symmetry of this tensor indicates that the deformation of the rock mass due to the orthorhombic fault sets is irrotational $\boldsymbol{\Omega} = \boldsymbol{O}$, as we have so assumed. Therefore, from Eq. (2.10), we obtain the infinitesimal strain tensor

$$\boldsymbol{\varepsilon} = 4\gamma \begin{pmatrix} n_1 s_1 & 0 & 0 \\ 0 & n_2 s_2 & 0 \\ 0 & 0 & n_3 s_3 \end{pmatrix}. \tag{11.27}$$

We have defined the coordinate system parallel to the principal axes of strain. Hence, from Eq. (11.27) we have

$$\varepsilon_1 = 4\gamma n_1 s_1, \tag{11.28}$$

$$\varepsilon_2 = 4\gamma n_2 s_2, \tag{11.29}$$

$$\varepsilon_3 = 4\gamma n_3 s_3. \tag{11.30}$$

The volume conservation is expressed by

$$\varepsilon_1 + \varepsilon_2 + \varepsilon_3 = 0. \tag{11.31}$$

Table 11.1: Strain states and the parameters Φ_ε and k.

k	Φ_ε	Principal strains	Strain state
1	1	$\varepsilon_1 = \varepsilon_2$	Constrictional strain
0	1/2	$\varepsilon_2 = 0, \quad \varepsilon_1 = -\varepsilon_3$	Plane strain
–1/2	0	$\varepsilon_2 = \varepsilon_3$	Flattening strain

The principal strains are defined to satisfy $\varepsilon_3 \le \varepsilon_2 \le \varepsilon_1$. Therefore, $\varepsilon_1 \ge 0, \quad \varepsilon_3 \le 0$. The intermediate principal strain ε_2 has positive and negative signs depending on the strain of the rock mass. Now, we introduce the parameter

$$\Phi_\varepsilon = \frac{\varepsilon_2 - \varepsilon_3}{\varepsilon_1 - \varepsilon_3} \quad (0 \le \Phi_\varepsilon \le 1)$$

to indicate the shape of the strain ellipsoid. $\Phi_\varepsilon = 0$ and 1 designate flattening ($\varepsilon_3 = \varepsilon_2 < \varepsilon_1$) and constrictional ($\varepsilon_3 < \varepsilon_2 = \varepsilon_1$) strains, respectively. Φ_ε in-between indicates a triaxial strain ellipsoid, whereas $\Phi_\varepsilon = 1/2$ represents plane strain. Since Φ_ε is defined as the same form as the stress ratio (Eq. (4.5)), Φ_ε is convenient to envisage a strain ellipsoid. However, the parameter

$$k = \varepsilon_2/\varepsilon_1 \quad (-1/2 \le k \le 1) \tag{11.32}$$

is convenient for the following arguments. This is related with Φ_ε as

$$\Phi_\varepsilon = \frac{1+2k}{2+k}, \qquad k = -\frac{2\Phi_\varepsilon - 1}{\Phi_\varepsilon - 2}.$$

The correspondence between k and the strain states are shown in Table 11.1. The parameter k is controlled from outside the system.

From Eqs. (11.28) and (11.29), we have $\varepsilon_1 n_2 s_2 = \varepsilon_2 n_1 s_1$ and, using the parameter k, we obtain

$$k n_1 s_1 - n_2 s_2 = 0. \tag{11.33}$$

On the other hand, $\boldsymbol{n}$ and $\boldsymbol{s}$ satisfies the relations

$$n_1 s_1 + n_2 s_2 + n_3 s_3 = 0, \tag{11.34}$$

$$n_1^2 + n_2^2 + n_3^2 = 1, \tag{11.35}$$

$$s_1^2 + s_2^2 + s_3^2 = 1 \tag{11.36}$$

by definition. The total number of components of $\boldsymbol{n}$ and $\boldsymbol{s}$ is six, but Eqs. (11.33)–(11.36) designate that only two of them are free. Accordingly, here we choose n_1 and n_2 as the independent variables for the following argument. Eliminating s_2, s_3 and n_3 from Eqs. (11.33)–(11.36), we obtain

$$s_1 = \pm \sqrt{\frac{1 - n_1^2 - n_2^2}{1 - n_2^2 - n_1^2 \left[\left(\dfrac{1 - n_1^2}{n_2^2} \right) k^2 + 2k \right]}}. \tag{11.37}$$

The eliminated values s_2, s_3 and n_3 are calculated using the four equations, i.e., $\boldsymbol{s}$ is linked with $\boldsymbol{n}$ through the orthorhombic symmetry. Once the two variables n_1 and n_2 are specified, the fault activity to accommodate the prescribed strain is constrained.

The next problem is how the variables n_1 and n_2 are chosen. To solve this problem, we assume that the frictional resistance

$$\tau_{\mathrm{R}} = \tau_0 + (\tan\phi)\,\sigma_{\mathrm{N}} \tag{11.38}$$

works on a fault plane with the parameters τ_0 and ϕ common to all faults. Namely, while a fault is moving, the shear stress on the fault plane is equal to

$$\sigma_{\mathrm{S}} = \tau_{\mathrm{R}} \tag{11.39}$$

Note that the rock mass is assumed to be isotropic. Therefore, the principal axes of stress coincide with the coordinate system, and the normal and shear stresses satisfy the following relationship with principal stresses:

$$\sigma_{\mathrm{N}} = \boldsymbol{t}(\boldsymbol{n})\cdot\boldsymbol{n} = \sigma_1 n_1^2 + \sigma_2 n_2^2 + \sigma_3 n_3^2, \tag{11.40}$$

$$\sigma_{\mathrm{S}} = \boldsymbol{t}(\boldsymbol{n})\cdot\boldsymbol{s} = \sigma_1 n_1 s_1 + \sigma_2 n_2 s_2 + \sigma_3 n_3 s_3. \tag{11.41}$$

Rearranging Eqs. (11.33)–(11.41), we obtain

$$\left(\sigma_1-\sigma_3\right)\left(n_1 s_1 - n_1^2\tan\phi\right) + \left(\sigma_2-\sigma_3\right)\left(k n_1 s_1 - n_2^2\tan\phi\right) = \tau_0 + (\tan\phi)\sigma_3. \tag{11.42}$$

This relationship is satisfied when a fault is slipping.

We have assumed a uniform spacing between faults. Consider a set to have n faults within a cube that has a unit length of sides. If one of the faces of the cube is parallel to the faults, the spacing equals $1/n$. Since the engineering shear strain of the cube is γ, the displacement of each fault is γ/n. The cube deforms in a similar way to a deck of cards. The n faults move by the distance γ/n against the resisting force $\tau_{\mathrm{R}} \times$ (unit area) $= \tau_{\mathrm{R}}$. Therefore, the energy dissipation by the n faults within the unit volume of the cube is

$$w = \sigma_{\mathrm{S}}\gamma. \tag{11.43}$$

Combining Eqs. (11.28), (11.33), (11.34), (11.41) and (11.43), we obtain the total dissipation due to the four sets in a unit volume The four sets of faults dissipate in a unit volume of the rock mass

$$\begin{aligned}
4w = 4\sigma_{\mathrm{S}}\gamma &= 4\left(\sigma_1 n_1 s_1 + \sigma_2 n_2 s_2 + \sigma_3 n_3 s_3\right)\cdot\frac{\varepsilon_1}{4 n_1 s_1} \\
&= \left[\sigma_1 n_1 s_1 + \sigma_2 n_2 s_2 + \sigma_3 n_3 s_3 - (\sigma_3 n_1 s_1 + \sigma_3 n_2 s_2 + \sigma_3 n_3 s_3)\right]\frac{\varepsilon_1}{n_1 s_1} \\
&= \left[\left(\sigma_1-\sigma_3\right)n_1 s_1 + \left(\sigma_2-\sigma_3\right)n_2 s_2\right]\frac{\varepsilon_1}{n_1 s_1} \\
&= \left[(\sigma_1-\sigma_3) + (\sigma_2-\sigma_3)k\right]\varepsilon_1.
\end{aligned}$$

Accordingly, the total dissipation is proportional to the strain ε_1. Let us define the symbol W to denote the constant of proportionality

$$W = (\sigma_1 - \sigma_3) + (\sigma_2 - \sigma_3)k. \tag{11.44}$$

This is the dissipation for every incremental strain $\partial(4w)/\partial\varepsilon_1 = W$. Using $\Phi = (\sigma_2 - \sigma_3)/(\sigma_1 - \sigma_3)$ and $\Delta\sigma = \sigma_1 - \sigma_3$, Eq. (11.44) is rewritten as

$$W = (1 + \Phi k)\Delta\sigma \tag{11.45}$$

and Eq. (11.42) is rewritten as

$$\left[(1 + \Phi k)\, n_1 s_1 - \left(n_1^2 + \Phi n_2^2\right) \tan\phi\right] \Delta\sigma = \tau_0 + (\tan\phi)\sigma_3. \tag{11.46}$$

The friction is thought to be dependent on confining pressure (Eq. (11.38)), so we regard σ_3 as a variable controlled from outside this system instead of the confining pressure.

Since there are pre-existing fractures with various orientations in the rock mass, some of which are chosen as faults, then the faults that can be activated by the minimum differential stress may be chosen. The right-hand side of Eq. (11.46) and $\Delta\sigma$ are, by definition, positive in sign. In addition, the right-hand side is given. Hence, the minimization of $\Delta\sigma$ is achieved by determining the optimal combination of n_1, n_2 and Φ that maximizes the content of the brackets in the left-hand side of Eq. (11.46). We have the analytical solutions for the cases $k = -1/2$, 0 and 1.

Constrictional strain is represented by $k = 1$. Then, the stress tensor and the fault sets are expected to have axial symmetry. Therefore,

$$\sigma_1 = \sigma_2, \quad n_1 = n_2. \tag{11.47}$$

Substituting these into Eq. (11.37), we have

$$s_1 = \sqrt{\frac{1 - 2n_1^2}{2}}. \tag{11.48}$$

Substituting Eqs. (11.47) and (11.48) into Eqs. (11.45) and (11.46), we obtain

$$2\Delta\sigma = W, \tag{11.49}$$

$$2\Delta\sigma \left(n_1 \sqrt{\frac{1 - 2n_1^2}{2}} - n_1^2 \tan\phi \right) = \tau_0 + (\tan\phi)\sigma_3. \tag{11.50}$$

Therefore, the dissipation W is minimized when $\Delta\sigma$ is minimized (Eq. (11.49)). The optimal n_1 is obtained by maximizing the content of the parentheses in the left-hand side of Eq. (11.50). Solving the equation

$$\frac{\mathrm{d}}{\mathrm{d}n} \left(n_1 \sqrt{\frac{1 - 2n_1^2}{2}} - n_1^2 \tan\phi \right) = \sqrt{\frac{1 - 3n_1}{2(1 - 2n_1)}} - 2n_1 \tan\phi = 0,$$

and using Eqs. (11.47) and (11.48), we obtain the fault orientation and slip direction of the case of constrictional strain:

$$n_1 = \frac{1}{2}\sqrt{1-\sin\phi}, \quad n_2 = n_1, \quad s_1\frac{1}{2}\sqrt{1+\sin\phi}. \tag{11.51}$$

Plane strain is indicated by $k = 0$ and $\varepsilon_2 = 0$. Due to the symmetry,

$$n_2 = 0. \tag{11.52}$$

Combining Eqs. (11.37) and (11.52), we have

$$s_1 = \sqrt{1-n_1^2} \tag{11.53}$$

and combining Eqs. (11.45) and (11.46), we obtain

$$\Delta\sigma = W, \tag{11.54}$$

$$\Delta\sigma\left(n_1\sqrt{1-n_1^2} - n_1^2\tan\phi\right) = \tau_0 + (\tan\phi)\sigma_3. \tag{11.55}$$

$\Delta\sigma$ fluctuates with W, again. Similar to the above discussion, it is found that the minimum $\Delta\sigma$ requires

$$n_1 = \frac{\sqrt{2}}{2}\sqrt{1-\sin\phi}, \quad n_2 = 0, \quad s_1 = \frac{\sqrt{2}}{2}\sqrt{1-\sin\phi}. \tag{11.56}$$

Flattening is indicated by $k = -1/2$ and $\varepsilon_2 = \varepsilon_3$. Due to symmetry, we have

$$n_2 = n_3, \quad \sigma_2 = \sigma_3. \tag{11.57}$$

Combining Eqs. (11.35), (11.37) and (11.57),

$$n_1 = \sqrt{1-2n_2^2}, \quad s_1 = \sqrt{3(1-n_1^2)}. \tag{11.58}$$

In this case, we have

$$\Delta\sigma = W, \tag{11.59}$$

$$\Delta\sigma\left(n_1\sqrt{1-n_1^2} - n_1^2\tan\phi\right) = \tau_0 + (\tan\phi)\sigma_3. \tag{11.60}$$

$\Delta\sigma$ is minimized when

$$n_1 = \frac{\sqrt{2}}{2}\sqrt{1-\sin\phi}, \quad n_2 = \frac{1}{2}\sqrt{1+\sin\phi}, \quad s_1 = \frac{\sqrt{2}}{2}\sqrt{1+\sin\phi}. \tag{11.61}$$

Interestingly, the three cases have a common minimum differential stress, which is obtained from Eqs. (11.49)–(11.51), (11.54)–(11.56) and (11.59)–(11.61):

$$\Delta\sigma_{\min} = \frac{2\cos\phi}{1-\sin\phi}\left[\tau_0 + (\tan\phi)\sigma_3\right]. \tag{11.62}$$

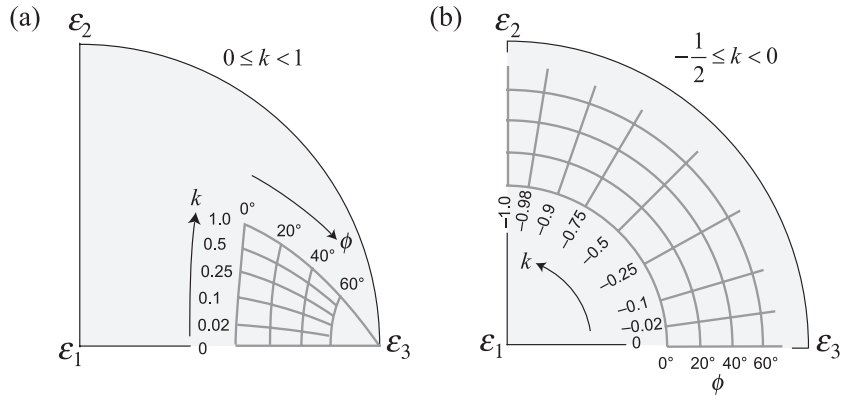

Figure 11.17: Equal-area projection showing the pole of the fault surfaces activated to accommodate a prescribed coaxial strain of the rock mass that includes the faults [194]. The pole of one of the orthorhombic fault sets is shown on a quadrant.

The resistance is assumed to be proportional to σ_3 (Eq. (11.38)), which is the substitution of confining pressure. The differential stress inherits the proportionality. The constant of proportionality equals $2\cos\phi\tan\phi/(1-\sin\phi)$. Substituting a representative value of rocks, e.g. $\phi = 35°$, we have $(\sigma_1 - \sigma_3) \propto 2.7\sigma_3$, i.e., σ_1 is about 1.7 times greater than σ_3.

The stress conditions and optimal fault sets were determined numerically for general triaxial strain cases $-1/2 < k < 0$ and $0 < k < 1$ by Reches [194]. It was found that the optimal parameters are continuous over the above intervals of k. Consequently, the optimal fault orientations and slip directions derived above are assembled into the equations

$$\begin{aligned} \boldsymbol{n} &= \frac{\sqrt{2}}{2}\left(\sqrt{\frac{(1-\sin\phi)}{1+k}},\ \sqrt{\frac{k(1-\sin\phi)}{1+k}},\ \sqrt{1+\sin\phi}\right)^{\mathrm{T}} \\ \boldsymbol{s} &= \frac{\sqrt{2}}{2}\left(\sqrt{\frac{(1+\sin\phi)}{1+k}},\ \sqrt{\frac{k(1+\sin\phi)}{1+k}},\ \sqrt{1-\sin\phi}\right)^{\mathrm{T}} \end{aligned} \tag{11.63}$$

for $0 \le k \le 1$ and

$$\begin{aligned} \boldsymbol{n} &= \frac{\sqrt{2}}{2}\left(\sqrt{1-\sin\phi},\ \sqrt{|k|(1+\sin\phi)},\ \sqrt{(1-|k|)(1+\sin\phi)}\right)^{\mathrm{T}} \\ \boldsymbol{s} &= \frac{\sqrt{2}}{2}\left(\sqrt{1+\sin\phi},\ \sqrt{|k|(1-\sin\phi)},\ \sqrt{(1-|k|)(1-\sin\phi)}\right)^{\mathrm{T}} \end{aligned} \tag{11.64}$$

for $-1/2 \le k < 0$.

The orientations of $\boldsymbol{n}$ and $\boldsymbol{s}$ predicted by Eqs. (11.63)–(11.64) are illustrated in Fig. 11.17. In the case of plane strain ($k = 0$), we have

$$\boldsymbol{n} = \frac{\sqrt{2}}{2}\left(\sqrt{1-\sin\phi},\ 0,\ \sqrt{1+\sin\phi}\right)^{\mathrm{T}}, \quad \boldsymbol{s} = \frac{\sqrt{2}}{2}\left(\sqrt{1+\sin\phi},\ 0,\ \sqrt{1-\sin\phi}\right)^{\mathrm{T}}, \tag{11.65}$$

indicating that all faults are parallel to the σ_2-axis and slip directions are perpendicular to this axis. Therefore, the four fault sets degenerate into a conjugate pair (Fig. 11.18(a)). Let θ be the angle between $\boldsymbol{n}$ and the σ_3-axis. This component is given in Eq. (11.65), and is rearranged as

$$
\begin{aligned}
n_3^2 &= \frac{1}{2}(1+\sin\phi) \qquad (11.66)\\
&= \left(\frac{\sqrt{2}}{2}\right)^2 \left(\overbrace{\cos^2\frac{\phi}{2}+\sin^2\frac{\phi}{2}}^{1} + \overbrace{2\sin\frac{\phi}{2}\cos\frac{\phi}{2}}^{\sin\phi}\right) = \left(\frac{\sqrt{2}}{2}\right)^2 \left(\cos\frac{\phi}{2}+\sin\frac{\phi}{2}\right)^2\\
&= \left(\cos\frac{\pi}{4}\cos\frac{\phi}{2}+\sin\frac{\pi}{4}\sin\frac{\phi}{2}\right)^2 = \cos^2\left(\frac{\pi}{4}-\frac{\phi}{2}\right) = \cos^2\left(\frac{\pi/2-\phi}{2}\right).
\end{aligned}
$$

Since n_3 is the direction cosine of $\boldsymbol{n}$, $\cos\theta = n_3$, we obtain

$$2\theta = \frac{\pi}{2} - \phi. \qquad (11.67)$$

This is identical to the shear plane angle predicted by the Coulomb-Mohr criterion (Eq. (6.4)). Consequently, plane strain leads to conjugate faulting.

As k departs from zero, faults make greater angles with σ_2-axis (Eqs. (11.63)–(11.64)), while the angle between $\boldsymbol{n}$ and ε_3-axis is constant for any $k \geq 0$. In this case, n_3^2 has the same form as the right-hand side of Eq. (11.66). Therefore, the constant angle equals θ in Eq. (11.67).

The angle between $\boldsymbol{n}$ and ε_1-axis is constant for any $k < 0$. Let θ' be the constant angle (Fig. 11.17). From Eq. (11.64), we have

$$
\begin{aligned}
n_1^2 &= \left(\frac{\sqrt{2}}{2}\right)^2 (1-\sin\phi) = \left(\frac{\sqrt{2}}{2}\right)^2 \left(\cos^2\frac{\phi}{2}+\sin^2\frac{\phi}{2}-2\sin\frac{\phi}{2}\cos\frac{\phi}{2}\right)\\
&= \left(\frac{\sqrt{2}}{2}\right)^2 \left(\cos\frac{\phi}{2}-\sin\frac{\phi}{2}\right)^2\\
&= \left(\sin\frac{\pi}{2}\cos\frac{\phi}{2}-\cos\frac{\pi}{2}\sin\frac{\phi}{2}\right)^2 = \sin^2\left(\frac{\pi}{4}-\frac{\phi}{2}\right) = \cos^2\left(\frac{\pi/2+\phi}{2}\right).
\end{aligned}
$$

Combining this and the equation $\cos\theta' = n_1$, we obtain $2\theta' = \pi/2 + \phi$. Therefore, we have Eq. (11.67) again, where $2\theta + 2\theta' = \pi$, i.e., $2\theta'$ is the supplementary angle of 2θ which is equal to $\angle$CBF in Fig. 6.5(a).

In the field, orthorhombic fault sets may be recognized by the fault-slip data shown in Fig. 11.17 and by the cross-cutting relationship between faults of different sets, which warrants the simultaneous activity of the fault sets. Krantz [104] identified orthorhombic fault sets in Jurassic sedimentary rocks. Reches [195] estimated the strain of a rock mass that encompasses a well-exposed system of orthorhombic fault sets, in good agreement with the theory.

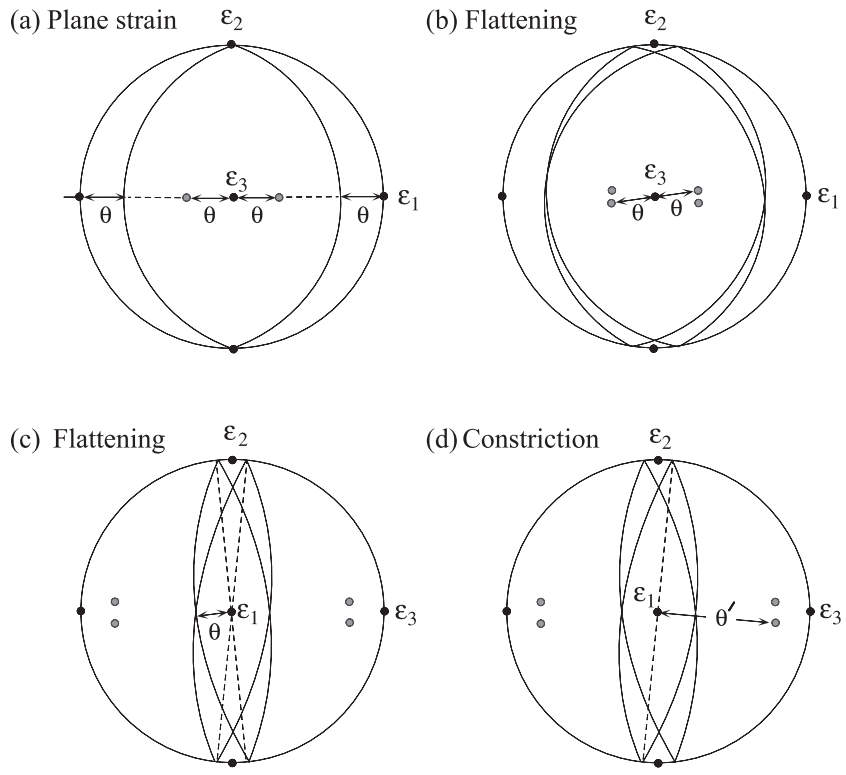

Figure 11.18: Fault sets accommodating a prescribed strain.

11.9 Block rotation and faulting

Highly deformed terrains have intricate fault systems, some of which were accompanied by the rotation of fault blocks, which is sometime indicated by curved fault striations[9]. Orogenic and accretionary belts may have rotated macroscale blocks. If fault activity was abruptly quenched in a rock mass, fault striations found in the mass may exhibit slip directions just before the end of the deformation. This section deals with a method to estimate a macro-deformation from internal mesoscale faults.

Instantaneous deformation is described by $\boldsymbol{L}\Delta t$, where $\boldsymbol{L}$ is the velocity gradient tensor and Δt is a short time interval. The tensor can be divided into two parts (Eq. (2.26)), indicating coaxial and rigid body rotation, $\boldsymbol{L} = \boldsymbol{D} + \boldsymbol{W}$. In the previous sections in this chapter, we have assumed that $\boldsymbol{W}$ is negligible compared to $\boldsymbol{D}$ for determining paleo stress or strain. If this is valid, it can be expected that an isotropic rock mass has a linear constitutive equation that links $\boldsymbol{D}$ and stress. However, it is

[9]Curved fault striations do not always indicate block rotations [224].

the present problem to incorporate the rotation in the fault striation analysis.

To this end, the Twiss-Protzman-Hurst model utilizes the *mechanics of micropolar continua* [249]. Micropolar continua are physically idealized macroscopic continua that have microscopic rigid particles and can model such substances as liquid crystals, rigid suspensions, concrete with sand, and muddy fluids. Within the present context, the rigid particles simulate fault blocks that can rotate. The mechanics of micropolar continua is beyond the scope of this book. Interested readers can consult textbooks [58, 128]. Here, the results of the Twiss-Protzman-Hurst model is briefly introduced [249].

Micropolar continua is a limited version of micromorphic continua that has deformable microstructures. The mechanics of micromorphic continua has macro and micro fields of kinematic variables including position, velocity, and rotation. The macro velocity gradient tensor is written as usual: $\overline{\boldsymbol{L}} = \overline{\boldsymbol{D}} + \overline{\boldsymbol{W}}$. The micro velocity gradient tensor is also defined as $\boldsymbol{L} = \boldsymbol{D} + \boldsymbol{W}$, i.e., we distinguish macro and micro quantities by overlines. Fault blocks are assumed to be rigid so that we use the mechanics of micropolar continua. Then we have $\boldsymbol{D} = \boldsymbol{O}$, and the micro velocity gradient tensor equals the micro spin tensor ($\boldsymbol{L} = \boldsymbol{W}$). Here, the principal values of $\overline{D}$ are numbered in descending order, $\overline{D}_1 \geq \overline{D}_2 \geq \overline{D}_3$. Obviously,

$$\frac{1}{2}\Delta\overline{D} \equiv \frac{1}{2}\left(\overline{D}_1 - \overline{D}_3\right)$$

is the maximum shearing rate, just like the maximum shear stress equals half the differential stress. The dimensionless quantity

$$\Phi_D \equiv \frac{\overline{D}_2 - \overline{D}_3}{\overline{D}_1 - \overline{D}_3} \qquad (0 \leq \Phi_D \leq 1)$$

designates the shape of the instantaneous strain ellipsoid. Here, elongation is positive so that $\Phi_D = 0$ and 1 indicate constriction and flattening, respectively. $\Phi_D = 1/2$ corresponds to plane strain.

Taking the principal axes of $\overline{\boldsymbol{D}}$ to define the rectangular Cartesian coordinates O-123, the maximum shear rate is on the O-13 plane. The non-diagonal components of a spin tensor make up a vorticity vector (Eq. (2.43)), and the vorticity is related to an angular velocity (Eq. (2.44)). The macro and micro angular velocities within the O-13 plane are equal to $\overline{W}_{13}$ and W_{13}, respectively. The quantity $\left(\overline{W}_{13} - W_{13}\right)$ indicates the difference in the velocities. Accordingly, we define the dimensionless number

$$\Omega \equiv \frac{\overline{W}_{13} - W_{13}}{\Delta\overline{D}/2}$$

to indicate the difference.

Let $\boldsymbol{N}$ be the outward unit normal to a small part on the surface of a fault block. The surface is rubbed by the relative velocity of the surface of the neighboring block. Twiss *et al.* [249] derived the direction of the resultant striae, being parallel to the vector

$$\boldsymbol{v} = \begin{pmatrix} 1 - N_1^2 - \Phi_D N_2^2 \\ \Phi_D - N_1^2 - \Phi_D N_2^2 \\ -N_1^2 - \Phi_D N_2^2 \end{pmatrix}^{\mathrm{T}} \begin{pmatrix} N_1 \\ N_2 \\ N_3 \end{pmatrix} + \frac{\Omega}{2} \begin{pmatrix} N_3 \\ 0 \\ -N_1 \end{pmatrix}. \tag{11.68}$$

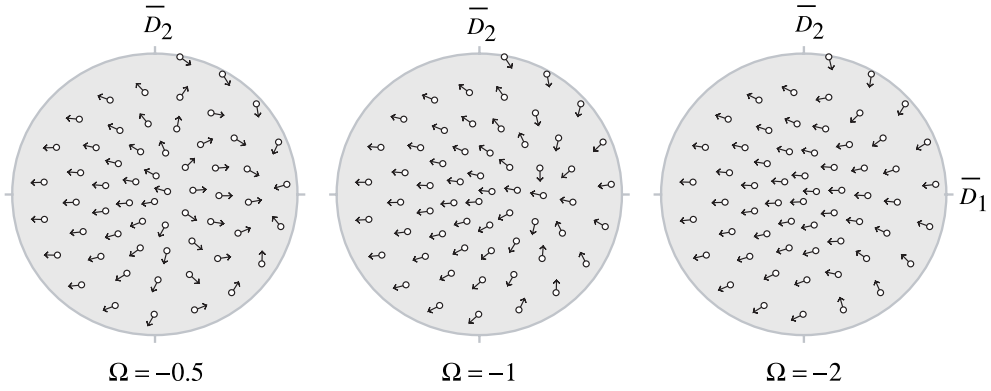

Figure 11.19: Tangent-lineation diagrams showing fault-slip data predicted by the Twiss-Protzman-Hurst model with different Ω and the same $\Phi_D = 0.5$ and the same principal axes of $\overline{\boldsymbol{D}}$ [249]. The $\overline{D}$-axis indicates the orientation of the maximum instantaneous elongation.

Given the dimensionless numbers Φ_D and Ω, the striating direction is calculated with this equation for any surface with $\boldsymbol{N}$. If the micro rotation is quenched by the cessation of macro deformation, the striation on the surface of fault blocks may give constraints to the kinematic parameters Φ_D and Ω and the principal orientations of $\overline{\boldsymbol{D}}$.

The fault-slip data predicted by this model is shown in Fig. 11.19. The tangent-lineation diagrams in Fig. 11.5 show the fault-slip data specifically for the case of $\Omega = 0$. When $|\Omega|$ is small, the gross pattern in the tangent-lineation diagram is similar to that of the case of $\Omega = 0$. However, it no longer has the orthorhombic symmetry but makes up a triclinic system. For a large Ω, arrows in the tangent-lineation diagram show a rotational pattern about $\overline{D}_2$-axis.

Exercises

11.1 Suppose a rock mass that is cut by a great number of conjugate sets of small-scale faults. Show that the strain of the mass caused by the internal fault activities is a plain strain. Assume that the orientation of stress axes does not change in the body, and that faulting are generated following the Coulomb-Navier criterion.

11.2 Show that the point S in Fig. 11.3 moves from S_0 to S_1 with an increase of Φ_B from 0 to 1, where the points S_0 and S_1 represent the orientation of the σ_1 and σ_3 axes, respectively, on the stereonet.

11.3 Verify that the σ_1-axis with a specific stress ratio Φ is constrained by a fault-slip datum to be in the region to the left of the dotted line in the stereonet in Fig. 11.7.